Supplementary Information

Structural basis of stepwise G protein activation by the viral chemokine receptor US28

Kevin M. Jude, Carl-Mikael Suomivuori, Deepa Waghray, Shoji Maeda, Yoshinori Fujiyoshi, Asuka Inoue, K. Christopher Garcia, and Naotaka Tsutsumi

Correspondence:

tsutsumi.naotaka@tmd.ac.jp (N.T.)

kcgarcia@stanford.edu (K.C.G.)

iaska@tohoku.ac.jp (A.I.)

carl-mikael.suomivuori@yale.edu (C.-M.S.)

Supplementary Discussion

General 3D classification strategy and interpretation of the C-state variants

In the $CX_3CL1.44$-US28-G_q structures, the globular body of the $CX_3CL1.44$ chemokine exhibited flexibility (Supplementary Fig. 2), a feature commonly observed in the wild-type CX_3CL1-US28 complex[1] and human chemokine receptor systems[2,3]. In contrast, the engineered N-terminal seven residues of the chemokine were well-defined. Therefore, to maximize the resolution of the US28-G_q interface, our primary 3D refinements were performed with all monomeric particles, regardless of heterogeneity in the chemokine density. When a subclass of particles showed the chemokine body in a metastable conformation, we also generated a separate reconstruction to visualize its position (Supplementary Fig. 2,3).

The C-state US28-G_q interface also exhibited flexibility, where we focused on the particle subset that yielded the highest-resolution features. The stochastic motion suggests that US28 can move further away from the Gβ interface, which leads to a more exclusive interaction with the extended α5 helix, and may represent a mechanism to ensure swift dissociation of the complex upon GTP binding.

Among the C-state variants, the class with closed AHD, termed the C'-state, was also identified from the 3D classification that identified the T2C-state, and refined to 2.9 Å resolution. Thus, it resembles the T2C-state with a closed AHD but lacks a clear GDP density (Supplementary Fig. 5c). Given its higher local conformational similarity to the C-state around the nucleotide-binding site, it most likely represents a state arising from stochastic AHD closure after C-state formation[4], although it could alternatively represent an intermediate between the T2C- and C-states. For the T2C- and C'-states, key regions were locally refined to guide model building (Supplementary Fig. 2).

Detailed structural analysis of the US28-G_q interfaces

State-dependent interactions at the $G\alpha_q$-αN helix

The engagement of US28 with the $G\alpha_q$-αN helix shifts dynamically during the activation trajectory (Fig. 4a and Supplementary Fig. 7). In the E-state, US28 recognizes a more N-terminal region of αN. Specifically, the $G\alpha_q$-Arg30 sidechain contacts the US28-Val141 sidechain and US28-

Gln65 Cα, while the $G\alpha_q$-Arg34 sidechain forms a hydrogen bond with the US28-Tyr138 backbone carbonyl and the $G\alpha_q$-Arg37 sidechain interacts with the Tyr138 sidechain. As the complex transitions, the interface shifts to a more C-terminal region in the subsequent states: in the T2C-state, the $G\alpha_q$-Arg37 guanidinium group shifts slightly to stack on the face of US28-Tyr138 while $G\alpha_q$-Arg38 engages the edge of US28-Tyr138, and in the C-state, $G\alpha_q$-Arg38 additionally forms a hydrogen bond with the US28-Met136 backbone carbonyl.

This interaction mode in the C-state complex is distinct from that of typical human chemokine receptors. Due to its shorter ICL2, US28 sits more shallowly within the $G\alpha_q$ crevice (formed by the α5 helix, αN-β1 junction, and β2-β3 loop) and therefore does not engage it as deeply. This distinction is important because the αN-β1 junction is one of the major sensors for receptor activation, and the connected β1-β3 sheet serves as a communication hub to activate the G protein[5].

Detailed rearrangements at the $G\alpha_q$-α5 helix

The most substantial interface remodeling occurs at the $G\alpha_q$ C-terminus, driven by the formation and rotation of the α5 helix (Fig. 4a and Supplementary Fig. 7). This movement pivots around the $G\alpha_q$-Val(-1) (where -1 is the extreme C-terminus; preceding positions are -2, -3, etc.) residue, which serves as a conserved anchor point. This C-terminal anchor is stabilized by the interaction of the carboxylate with the N-terminal dipole of US28 H8, which unwinds slightly in the T2C and C states to donate hydrogen bonds from the backbone and sidechain of US28-Thr296. The interactions of the preceding Asn(-3) residue, however, are state-dependent. In the E-state, its sidechain forms a single hydrogen bond with the US28-Arg129 sidechain. In contrast, in the C-state, it forms an extensive hydrogen bonding network with the backbones of TM7 and the TM7-H8 turn. The Tyr(-4) sidechain also undergoes a marked rearrangement of its interactions. In the E-state, its hydroxyl group forms hydrogen bonds with US28-Ser67 and -Gly68. In the T2C- and C-states, however, the sidechain reorients such that its aromatic ring is sandwiched between US28-Cys66/Arg129 and is ultimately stabilized in the C-state by a thiol-π interaction, while the positive quadrupole of the ring edge is oriented toward the side chain carboxylic acid of US28-Asp128. The engagement at the base of the intracellular pocket is also state-dependent. In the E-state,

the Leu(-9) residue is lodged at the pocket's edge on ICL3, anchored by both a backbone-backbone hydrogen bond and sidechain hydrophobic interactions with US28-Q219. In the T2C- and C-states, however, the interface rearranges, allowing the Asp(-14) residue to insert deeper into this pocket (Fig. 4a). Consequently, the formation of the α-helix draws a C-terminal segment of $G\alpha_q$, previously positioned outside the pocket in the E-state, into the intracellular cleft. This engagement facilitates the formation of numerous new hydrophobic and polar interactions (Supplementary Fig. 7).

Comparison between the C-state US28 complexes with G_q and G_i

Interestingly, the previously identified C-state US28-G_i structure retains a US28-mediated bridge between $G\alpha_i$ and Gβ, a feature attributed to a unique bend in its α5 helix[1]. We propose that the relaxation of this bending strain would straighten the α5 helix and cause a slight rotational displacement of the G protein (Fig. 3d), resulting in the predominantly US28-Gα interface observed in the current G_q complex. Therefore, the newly resolved C-state $CX_3CL1.44$-US28-G_q complex represents a more canonical and fully active conformation compared to that of the US28-G_i complex. This structural difference likely underlies a reduced GEF activity of US28 toward G_i compared to $G_{q/11}$ (ref [1]).

Structural determinants in G protein subtype selectivity by US28

Our structures of the signaling-competent, authentic C-state US28-G_q complex provide a structural framework to understand the G protein subtype selectivity of US28, which is known to couple to G_q, $G_{12/13}$, and G_i, but not G_s[6,7]. A comparison of the C-terminal sequences of Gα subunits, which primarily determine the coupling specificity, shows a key difference, where $G\alpha_s$ uniquely possesses a glutamate residue at the -3 position (Supplementary Fig. 10a). To visualize the structural consequence of this residue, we generated a homology model of the US28-$G\alpha_s$ complex based on the C-state US28-G_q structure[8].

The homology model predicts significant electrostatic repulsion between the negatively charged sidechain of $G\alpha_s$-Glu(-3) and the backbone carbonyls at the intracellular end of US28 TM7. This contrasts with the favorable interactions observed in the C-state US28-G_q complex and

the accommodation of the smallest sidechain in the US28-G_i complex (Supplementary Fig. 10b,c). While $G\alpha_s$ could be compatible with the E-state by interacting with US28-Arg129, this clash in the C-state would likely prevent the stable engagement required for G protein activation.

This predicted inhibitory mechanism in US28 contrasts with the established mode of G_s coupling by prototypical G_s-coupled receptors, such as β2AR[9] (Supplementary Fig. 10b,c). In the active β2AR-G_s complex structure, TM6 undergoes a much larger outward displacement compared to that of US28. This wider opening of the intracellular cavity repositions the $G\alpha_s$ C-terminus, placing the Glu(-3) residue at the periphery of the binding interface rather than at its core. In this conformation, the Glu(-3) sidechain makes minimal direct contact with the receptor and is instead accommodated by weak interactions between TM6 and TM7. Therefore, the more compact intracellular architecture of US28 provides a structural basis for its inability to couple with G_s, offering a clear mechanism for its G protein selectivity.

This structural constraint imposed by a relatively narrow intracellular opening may also explain the G protein coupling profiles of endogenous human chemokine receptors[10,11]. These receptors predominantly signal through $G_{i/o}$, which has the least bulky C-terminal region, and show some coupling to $G_{q/11}$ and $G_{12/13}$ subtypes but generally exclude G_s[10].

Structural basis for G protein-biased agonism by engineered chemokines

The $CX_3CL1.44$-US28 structure determined here allows us to compare the structures of US28 bound to three different CX_3CL1 variants, including the crystal structure of $CX_3CL1.35$-US28 (Supplementary Fig. 11a-d). Notably, the N-terminal peptides of the wild-type CX_3CL1 and its G protein-biased variants, $CX_3CL1.35$ and $CX_3CL1.44$, each trace a unique path at CRS2.

The N-terminal peptide of $CX_3CL1.44$ forms an α-helix, allowing it to project sidechains into both the major and minor ligand-binding pockets. The peptide of $CX_3CL1.35$, while lacking a defined secondary structure, also engages both pockets. In contrast, the unstructured N-terminal peptide of the wild-type CX_3CL1 interacts solely with the minor pocket. The interaction at the major pocket induces displacement of TM5 and TM6. Furthermore, a critical difference is observed at CRS3. The wild-type chemokine, which is endogenously β-arrestin-biased, establishes extensive contacts between the chemokine globular core and receptor extracellular

loop (ECL) 2 at CRS3 (Supplementary Fig. 11e). This interaction, which appears to induce a downward conformational change in ECL2, is absent in the two G protein-biased engineered variants.

Therefore, we propose a two-part mechanism for the G protein-selective activation of US28: (1) the simultaneous engagement of both the major and minor binding pockets by the chemokine's N-terminal peptide, and (2) the absence of the specific CRS3-mediated interaction that repositions ECL2.

Supplementary Table 1 | Cryo-EM data collection and refinement statistics

	E-state		T2C-state		C'-state		C-state	
	CX_3CL1 core unmodeled	CX_3CL1 core modeled	CX_3CL1 core unmodeled with GDP		CX_3CL1 core unmodeled without GDP		CX_3CL1 core unmodeled	CX_3CL1 core modeled
	global	global	global	local	global	local	global	global
EMDB ID (EMD-)	**66864**	**66942**	**66923**	N/A	**66930**	N/A	**66922**	**66928**
PDB ID	**9XH2**	**9XJP**	**9XIY**	N/A	**9XJ7**	N/A	**9XIX**	**9XJ5**
Map	1	2	5-1	5-2/5-3	6 -1	6-2/6-3	3	4
Nominal mag.	**105,000x**							
Calibrated mag.	**57,624x**							
Voltage (kV)	**300**							
Exposure(e/Å^2)	**50**							
Defocus range (μm)	**-0.8 to -2.0**							
Pixel size (Å)	**0.8677**							
Symmetry	**C1**							
Initial particle no.	**8,400,483**							
Final particle no.	193,867	64,658	70,394	US28/G_q 69,802/ 69,799	69,523	US28/G_q 68,903/ 68,894	268,599	89,862
Resolution (Å)								
FSC=0.143 (masked)	2.6	2.7	2.9	3.5/3.2	2.9	3.4/3.2	2.6	2.8
Sharpening *B* (Å^2)*	-78.3	-68.1	-40	-88.5/-84.7	-73.4	-86.5/-81.3	-86.4	-75.3
Model								
Initial model	PDB: 7RKF, AlphaFold3	PDB: 7RKF, AlphaFold3	E-state model	N/A	T2C-state model	N/A	PDB: 7RKF, AlphaFold3	PDB: 7RKF, AlphaFold3
Resolution (Å)								
FSC = 0.5 (masked)	2.8	2.9	3.2		3.2		2.8	3.0
Model composition								
Non-H atoms	10,161	10,700	10,005		10,068		9,083	9,554
Protein residues	1,277	1,343	1,260		1,270		1,152	1,213
Ligands	GDP/CLR	CLR	GDP		N/A		N/A	N/A
B factors (Å^2)								
Protein	48.0	44.2	110.79		68.1		55.5	58.6
Ligand	25.9/49.0	62.4	59.60		N/A		N/A	N/A
R.m.s. deviations								
Bond lengths (Å)	0.003	0.003	0.002		0.003		0.003	0.003
Bond angles (°)	0.550	0.508	0.453		0.544		0.537	0.551
Validation								
MolProbity score	1.68	1.48	1.58		2.00		1.41	1.74
Clashscore	3.76	3.43	4.02		6.85		3.16	4.16
Rotamer outliers (%)	3.54	2.77	2.39		4.01		2.42	3.46
Ramachandran plot								
Favored (%)	97.55	97.97	97.50		97.05		97.97	97.32
Allowed (%)	2.45	2.03	2.50		2.87		2.03	2.68
Disallowed (%)	0	0	0		0.08		0	0
EMRinger score	3.14	3.57	2.18		2.58		3.47	3.21

*Uniformly sharpened with indicated *B* factors for Phenix refinement and/or local map visualization. DeepEMhancer sharpened for overall map representation.

Supplementary Table 2 | Molecular Dynamics simulations checklist

Reliability and reproducibility checklist for molecular dynamics simulations ***All boxes must be marked YES by acceptance unless an N/A option is available**	**Yes**	**N/A**	**Response** **(Please state where this information can be found in the text)**
1. Convergence of simulations and analysis			
1a. Is an evaluation presented in the text to show that the property being measured has equilibrated in the simulations (*e.g.* time-course analysis)?	☒		Time-course analyses are presented in Supplementary Fig 6.
1b. Then, is it described in the text how simulations are split into equilibration and production runs and how much data were analyzed from production runs?	☒		Yes (in Methods).
1c. Are there at least 3 simulations per simulation condition with statistical analysis?	☒		16 independent simulations were run under a single condition (statistical analysis not applicable).
1d. Is evidence provided in the text that the simulation results presented are independent of initial configuration?	☒		16 simulations with independent equilibration were performed, and these produced distinct trajectories but with consistent results (see Results and Methods as well as Fig. 3 and Supplementary Fig. 6).
2. Connection to experiments			
2a. Are calculations provided that can connect to experiments (*e.g.* loss or gain in function from mutagenesis, binding assays, NMR chemical shifts, J-couplings, SAXS curves, interaction distances or FRET distances, structure factors, diffusion coefficients, bulk modulus and other mechanical properties, *etc.*)?	☒		Simulations results are compared to experimental structures (Fig. 3 and Supplementary Fig. 6).
3. Method choice			
3a. Is it described in the text what force field and water model are used and why?	☒		Yes (in Methods).
3b. Do simulations contain membranes, membrane proteins, intrinsically disordered proteins, glycans, nucleic acids, polymers, or cryptic ligand binding?	☒	☐	
If 3b is **YES**, are enhanced sampling methods used?	☐	☒	
If enhanced sampling methods are used, are the convergence criteria clearly stated?	☐		
If 3b is **YES**, is it explained in the text why or why not enhanced sampling methods are used?	☒		Yes (in Methods).
4. Code and reproducibility			
4a. Is a table provided describing the system setup, such as simulation box dimensions, total number of atoms, total number of water molecules, salt concentration, lipid composition (number of molecules and type)?	☒		Yes (Supplementary Table 3).
4b. Is it described in the text what simulation and analysis software and which versions are used?	☒		Yes (in Methods).
4c. Are initial coordinate and simulation input files and a coordinate file of the final output provided as supplementary files or in a public repository?	☒		These are provided in a Zenodo repository [https://doi.org/10.5281/zenodo.20598927] under entry 20598927.
4d. Is there custom code or custom force field parameters?	☐	☒	Response not needed if **N/A**
If **YES**, are they provided as supplementary profiles or in a public repository?	☐		

Supplementary Table 3 | Summary of simulation setup.

initial dimensions	130 Å × 130 Å × 195 Å
atoms	309,986
waters	76,959
lipids	453 POPC
neutralizing salt	0.15 M KCl

*System setup for all 16 simulations started from the T2C-state.

Simulation lengths are listed in Supplementary Fig 6.

Supplementary Table 4 | Summary of structure-guided mutagenesis at the US28-G_q interface.

Mutant	State-dependence of contact	Structural hypothesis	Expression [%WT(1:1) ± SEM]	LogRAi [mean ± SEM]	*P*-value	Number of independent experiments
R129$^{3.50}$A	Persistent across all states	Primary anchor for G protein and essential for active US28 conformation	73.3 ± 10.8	ND (Completely abolished)	ND	3
D128$^{3.49}$A	Persistent across all states	Maintains interaction with Tyr(-4) of $G\alpha_q$ C-terminus throughout activation	53.0 ± 2.9	-0.64 ± 0.16	0.0236 [vs. WT(1:2)]	4
S218$^{5.68}$A	Persistent across all states	Provides continuous structural support	79.8 ± 8.8	-0.67 ± 0.02	< 0.0001 [vs. WT(1:2)]	3
V294$^{7.56}$A	None (Allosteric)	Receptor stabilization via packing against V229$^{6.36}$	96.2 ± 9.5	-0.64 ± 0.21	0.0897 [vs. WT(1:1)]	3
K297$^{8.49}$A	Forms in T2C- and C-states	Supports later activation steps	76.3 ± 4.2	-1.00 ± 0.05	0.0004 [vs. WT(1:2)]	3
R221^{ICL3}A	Greatest in E-state, decreases in T2C-/C-states	Supports initial engagement	108.1 ± 9.5	-0.20 ± 0.01	0.0044 [vs. WT(1:1)]	3
S67$^{2.38}$A	Extensive in E-/T2C-states, decreases in C-state	Supports early activation steps	83.5 ± 2.9	-0.33 ± 0.06	0.0092 [vs. WT(1:1)]	4
I133$^{3.54}$A	Transiently increased in T2C-state	Selectively supports T2C-state	82.1 ± 7.0	-0.84 ± 0.04	0.0002 [vs. WT(1:1)]	4
R225$^{6.32}$A	Transiently increased in T2C-state	Selectively supports T2C-state	94.5 ± 4.2	-0.28 ± 0.05	0.0258 [vs. WT(1:1)]	3

ND: Not Determined.

Each independent experiment was performed in technical triplicate.

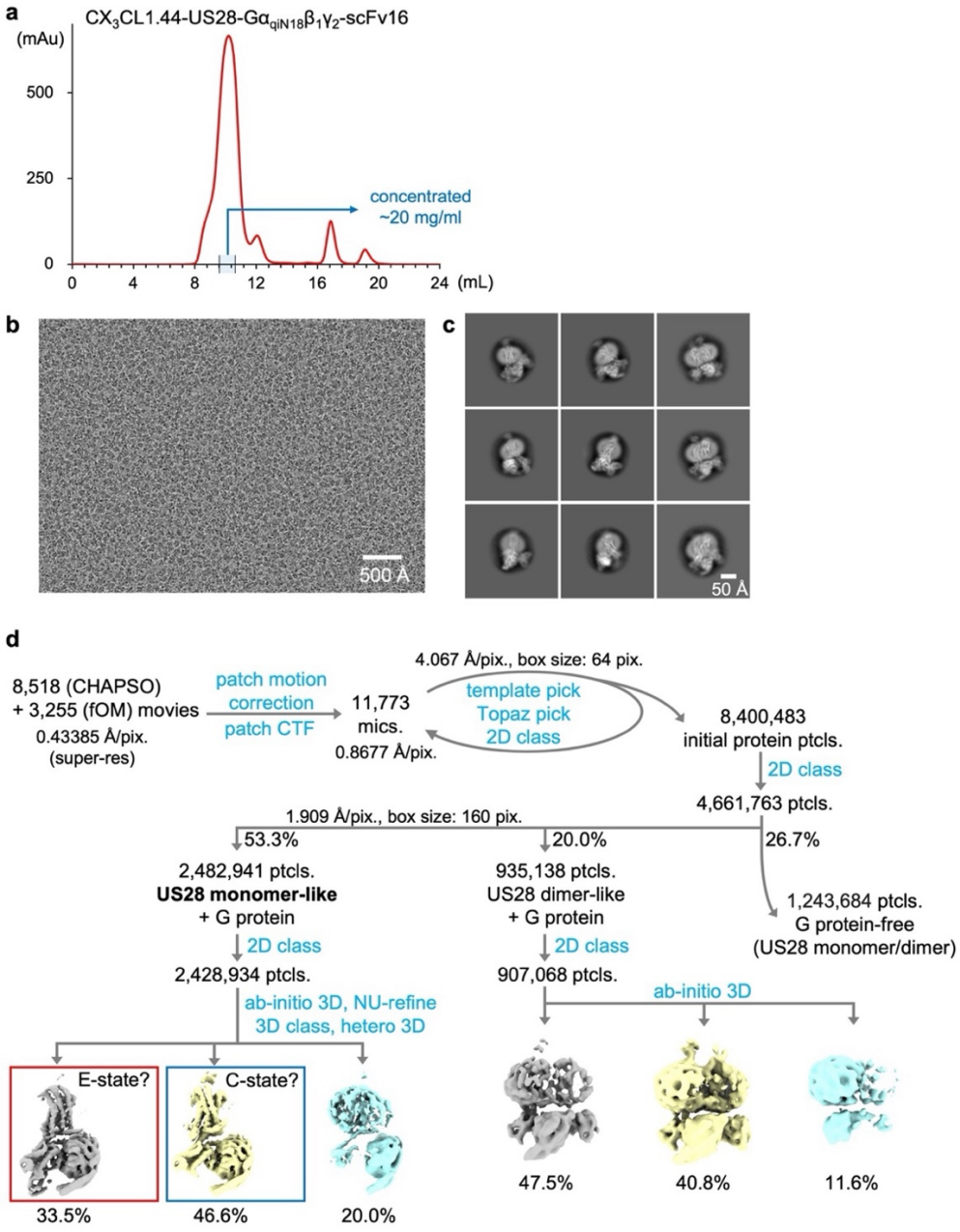

Supplementary Fig. 1| Purification of the $CX_3CL1.44$-US28-G_q complex and the initial cryo-EM data processing scheme.

a, Size-exclusion chromatography (SEC) profile of the purified $CX_3CL1.44$-US28-$G\alpha_{qiN18}\beta_1\gamma_2$-scFv16 complex. Source data are provided as a Source Data file. **b**, Representative cryo-EM micrograph (scale bar 500 Å) and **c**, selected 2D class averages (left, scale bar 50 Å). A low-resolution class average from datasets collected in thicker ice areas is also shown (bottom right), suggesting a potential 2:2 receptor-G_q complex in which two $CX_3CL1.44$ and two G_q molecules are visualized. **d**, Flowchart of the initial cryo-EM data processing. Movies collected from samples prepared with CHAPSO and fOM were jointly processed. Initial 2D and 3D classifications separated the dataset into US28 monomer-like, US28 dimer-like, and G protein-free populations. The monomer-like population showed initial heterogeneity corresponding to putative E-state and C-state conformations. Patch CTF: Patch CTF Estimation, template pick: Template Picker, Topaz pick: training and extraction by Topaz, 2D class: 2D Classification, ab initio 3D: Ab-Initio Reconstruction, NU-refine: Non-uniform Refinement, 3D class: 3D Classification, hetero 3D: Heterogeneous Refinement.

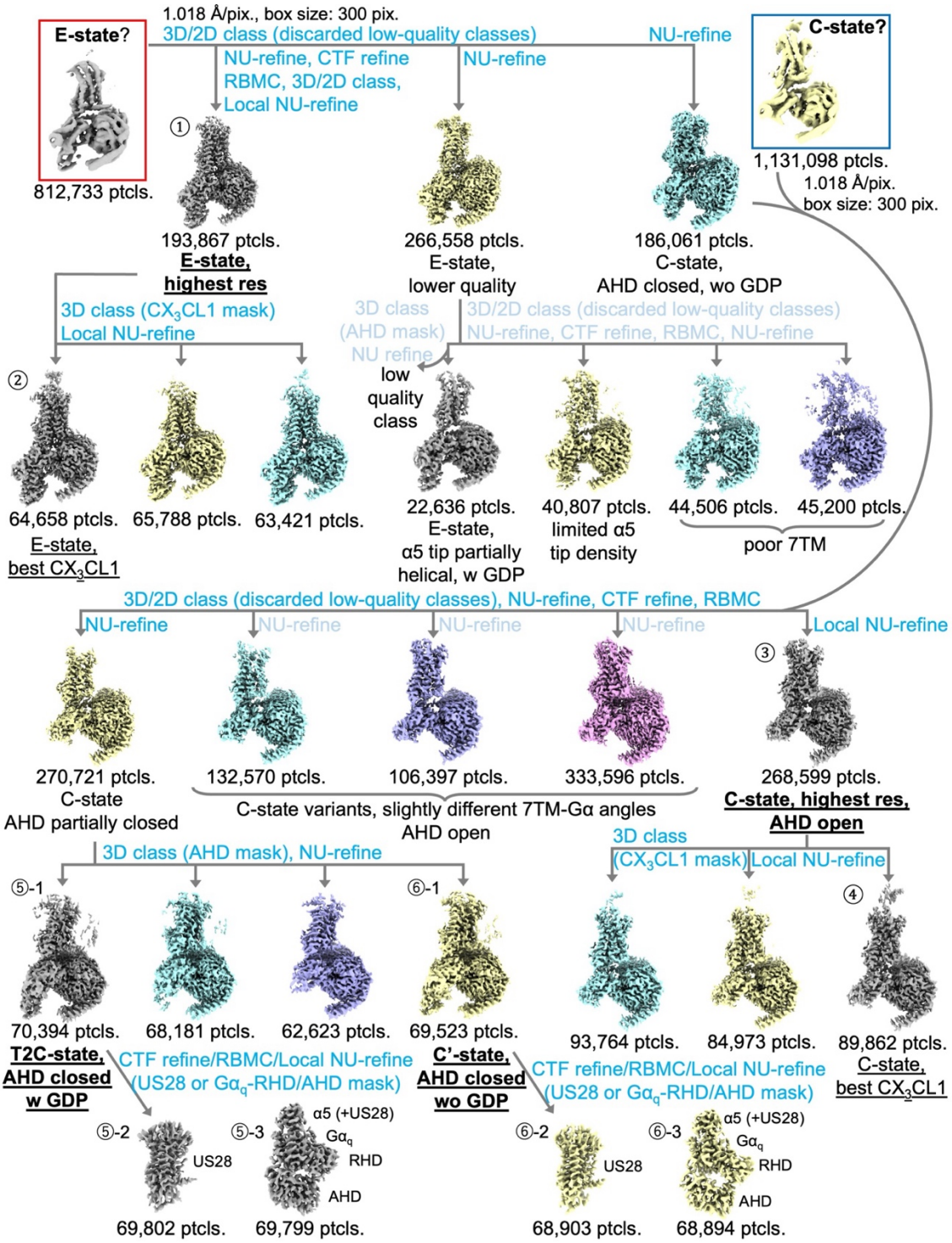

Supplementary Fig. 2| Detailed 3D classification workflow for the monomeric US28-G_q complex.
Flowchart detailing the iterative classification and refinement strategy for the monomeric particles. Starting from the initial E-state-like and C-state-like populations, extensive processing using 3D/2D classification, (local) NU-refine, CTF refinement, and RBMC was performed. This pipeline resolved the high-resolution structures for the E-state (1, 2), C-state (3, 4), T2C-state (5-1), and C'-state (6-1). Mask-focused classifications (e.g., on CX_3CL1 body or AHD) and local refinements (5-2, 5-3, 6-2, 6-3) were employed to resolve heterogeneity and improve map quality in specific regions. RBMC: Reference-Based Motion Correction, CTF-refine: Global and Local CTF refinement, Local NU-refine: Local Refinement with NU-refine.

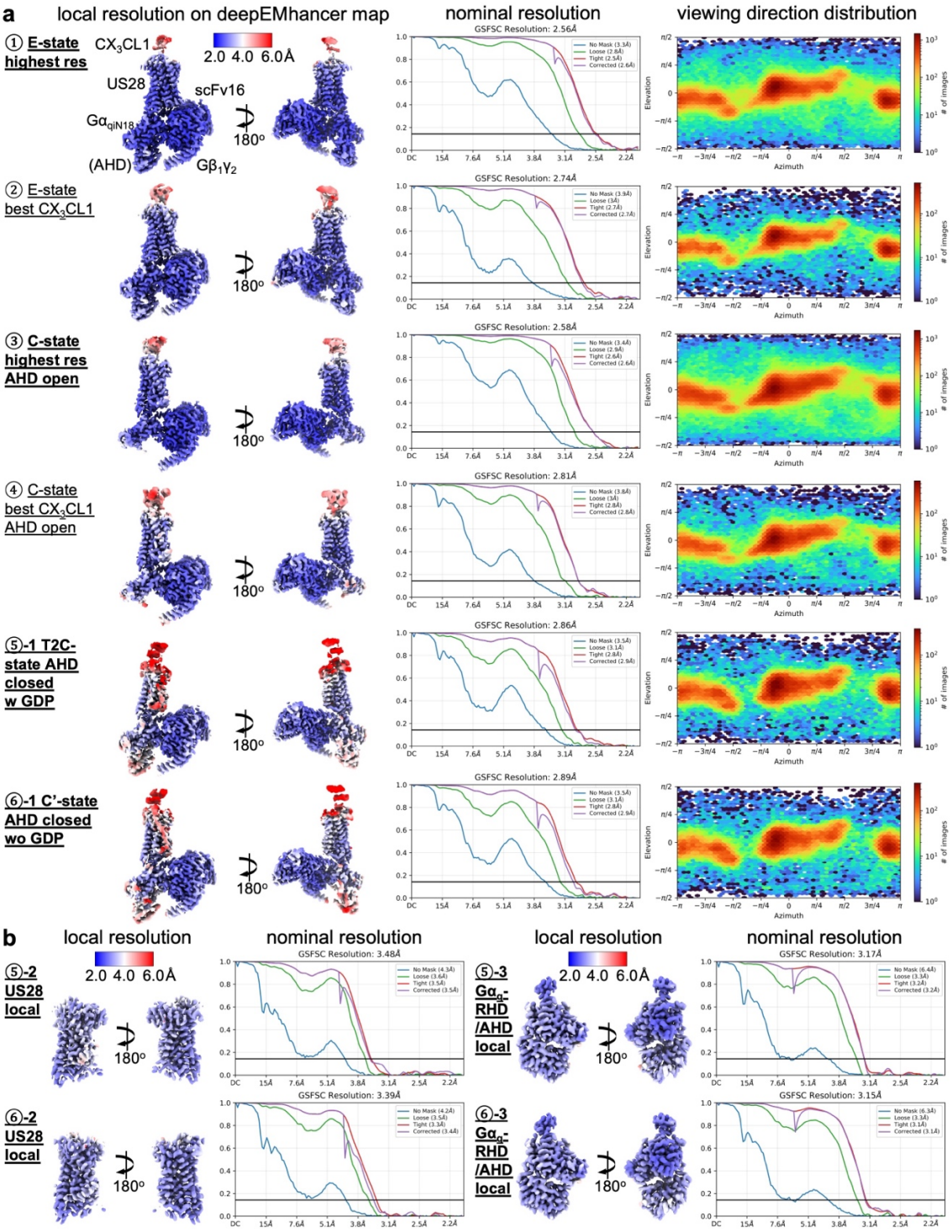

Supplementary Fig. 3| Quality assessment of the cryo-EM reconstructions.

a, Evaluation of the globally refined cryo-EM maps for the major conformational states: (1) E-state, highest resolution; (2) E-state, best CX_3CL1 core density; (3) C-state, highest resolution, open AHD; (4) C-state, best CX_3CL1 core density, open AHD; (5-1) T2C-state, closed AHD with GDP; and (6-1) C'-state, closed AHD without GDP. For each state, the local resolution map (colored on the deepEMhancer map), the gold-standard Fourier Shell Correlation (GSFSC) curve indicating the nominal resolution, and the viewing direction distribution plot are shown. **b**, Evaluation of the locally refined maps used as model building guides for the T2C-state (5-2: US28 local; 5-3: $G\alpha_q$-RHD/AHD local) and the C'-state (6-2: US28 local; 6-3: $G\alpha_q$-RHD/AHD local).

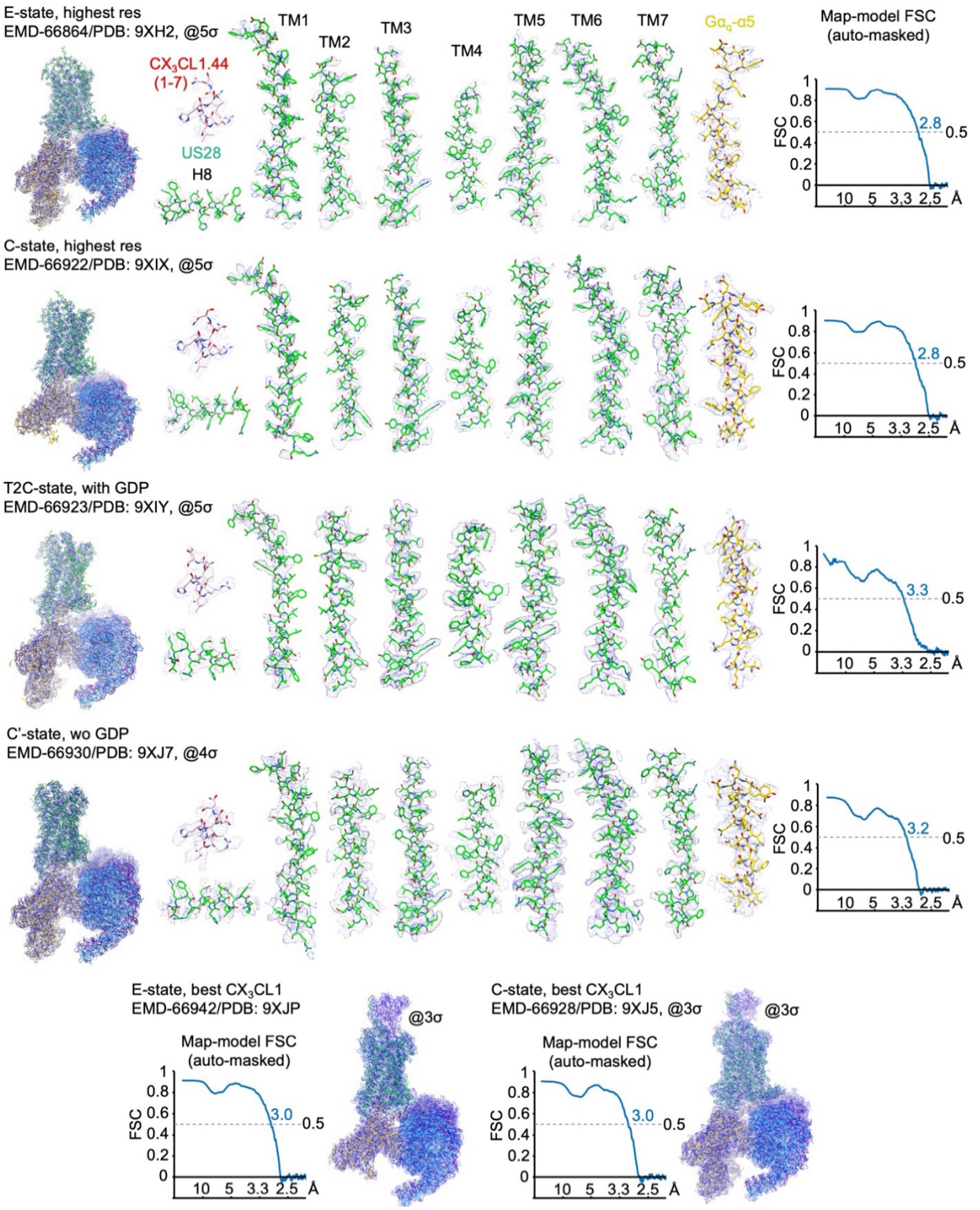

Supplementary Fig. 4 | Representative cryo-EM densities and model validation.
Representative cryo-EM densities (blue mesh) overlaid with the refined atomic models for the E-state, C-state, T2C-state, and C'-state. Densities are shown for key structural elements including the $CX_3CL1.44$ N-terminus (residues 1-7), US28 transmembrane helices (TMs) and helix 8 (H8), and the $G\alpha_q$-α5 helix. Maps are contoured at the indicated sigma (σ) levels. The map-versus-model Fourier Shell Correlation (FSC) curves (auto-masked) are shown for each state.

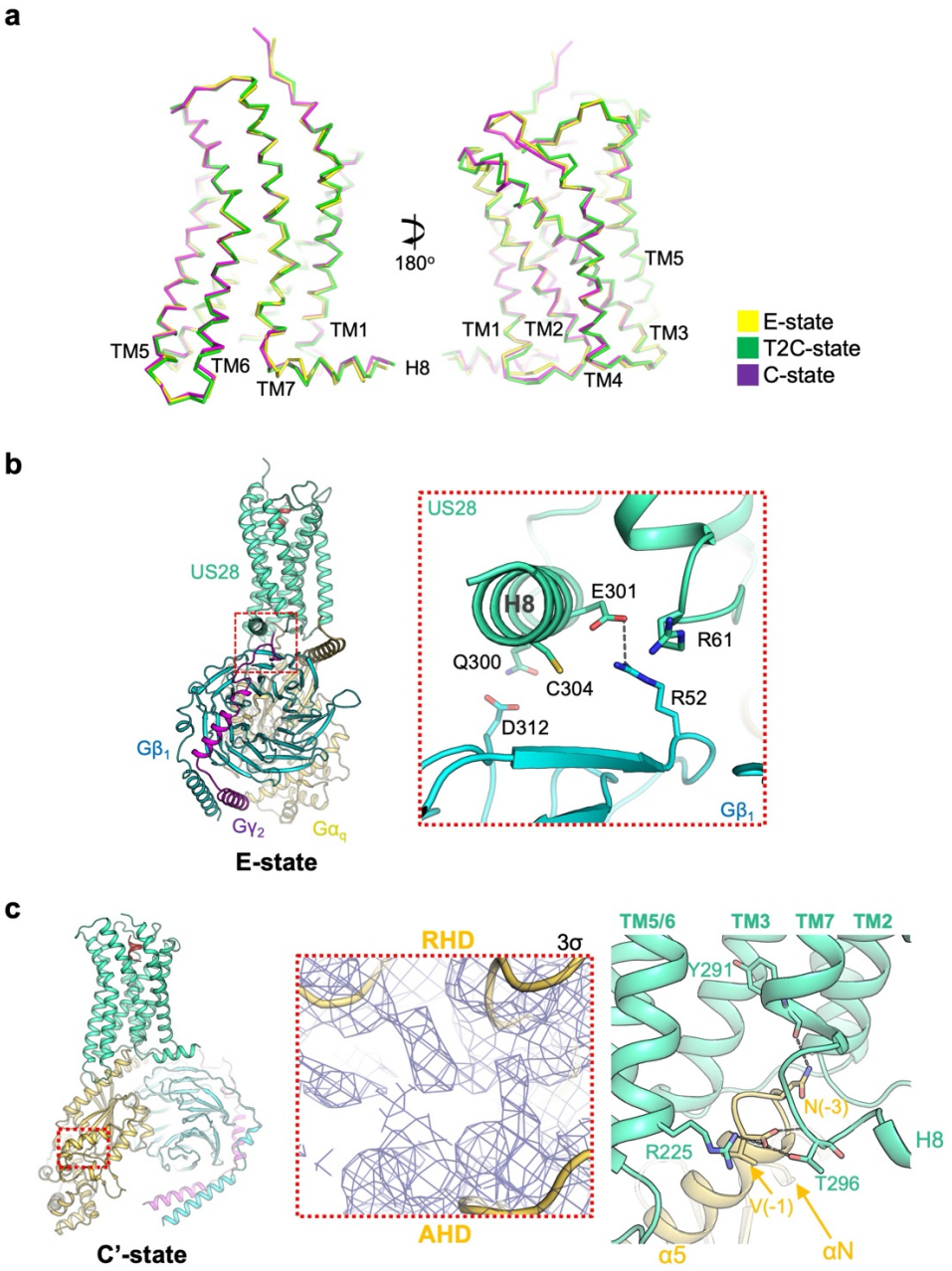

Supplementary Fig. 5 | US28 conformation across distinct G protein engaging states, interface between US28 and Gβ in the E-state, and overall view of the C'-state.

a, Structural alignment of US28 bound to G_q across the E-state (yellow), T2C-state (green), and C-state (purple). The receptors are represented as ribbon models. The structures exhibit a high degree of similarity with a global Cα RMSD of ~0.6 Å, demonstrating that US28 acts as a rigid catalytic scaffold during progressive G protein engagement, while subtle state-dependent conformational changes beyond the resolution limits of the current static cryo-EM maps cannot be formally excluded. **b**, Interface between US28 and Gβ in the E-state. Overall (left) and close-up (right) views of the US28-Gβ interface in the E-state. Contacting residues are shown as sticks and a salt bridge is indicated by the gray dashed line. **c**, Views of the nucleotide-binding pocket and interface between the US28 intracellular core (green-cyan) and the $G\alpha_q$ C-terminus (yellow) of the $CX_3CL1.44$-US28-G_q complex in the nucleotide-free C'-state. The panels show an overall view (left), a close-up of the nucleotide-binding pocket (middle), and the receptor-Gα C-terminus interface (right), in a layout analogous to Fig. 2b,d. Map contour level (σ) is indicated in the figure.

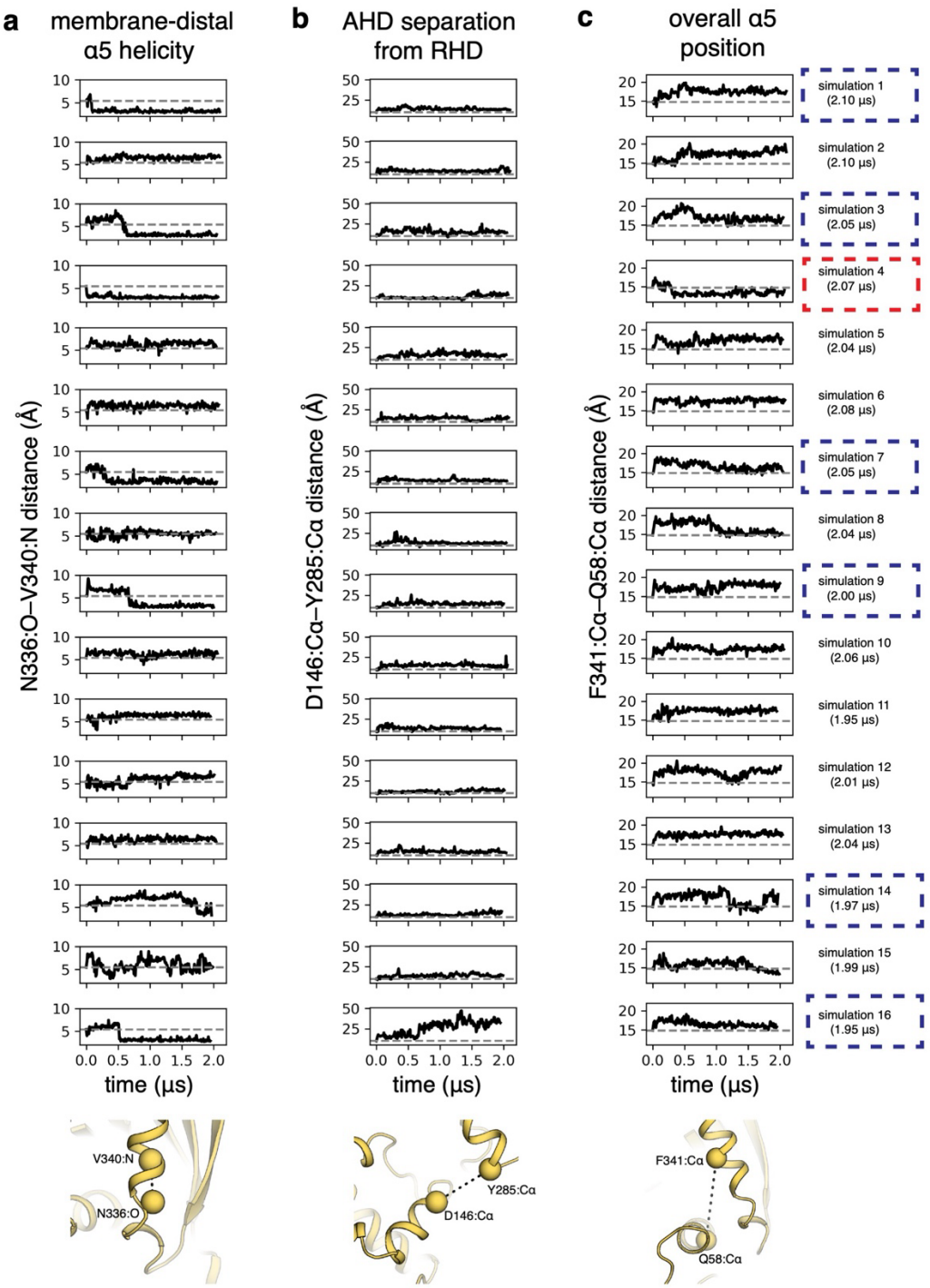

Supplementary Fig. 6 | Metrics used to monitor conformation of Gα in MD simulations.
These metrics, along with visual inspection, were used to identify conformational transitions. Simulations showing transitions toward the C-state are indicated by blue boxes, and the simulation showing a transition toward the E-state is indicated by a red box. **a**, Increased helicity in the membrane-distal region of the α5 helix is indicated by a decrease in the Asn336:O–Val340:N distance. **b**, AHD separation from the RHD is indicated by an increase in the Asp146:Cα–Tyr285:Cα distance. **c**, Movement of the α5 helix away from the membrane and toward GDP is indicated by a decrease in the Phe341:Cα–Gln58:Cα distance. Dashed horizontal lines represent values for the metric in the starting T2C-state structure. The renderings at the bottom of each panel show the relevant atoms in the starting structure for each metric. Source data are provided as a Source Data file.

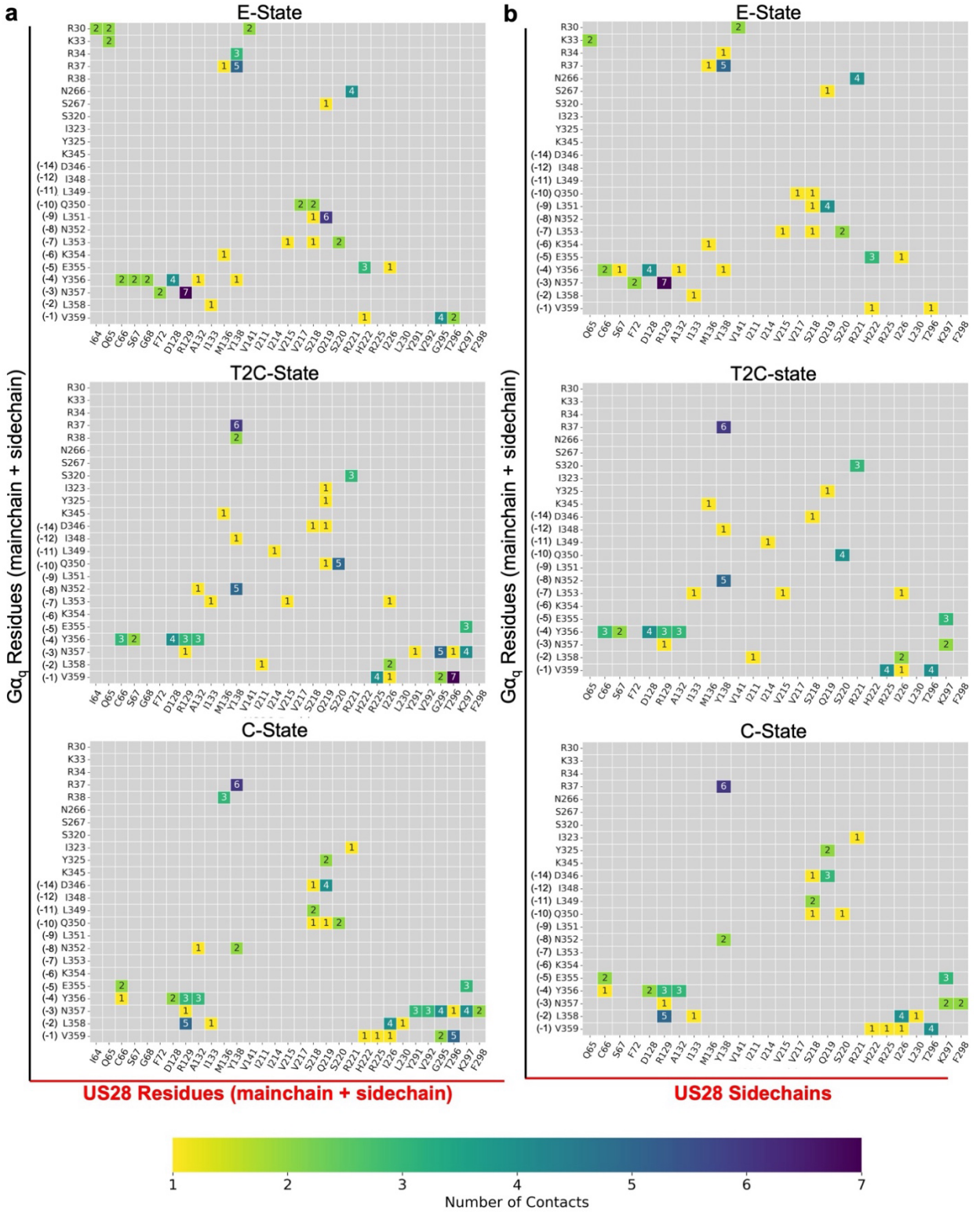

Supplementary Fig. 7 | State-dependent interaction networks at the US28-G_q interface.
Contact maps illustrating the detailed molecular interactions between US28 residues (x-axis) and $G\alpha_q$ residues (y-axis) across the three resolved states (E-state, T2C-state, and C-state). **a**, Interactions involving both mainchain and sidechain atoms of US28. **b**, Interactions involving only the sidechain atoms of US28. In all panels, the color intensity indicates the number of atomic contacts, as shown by the scale bar.

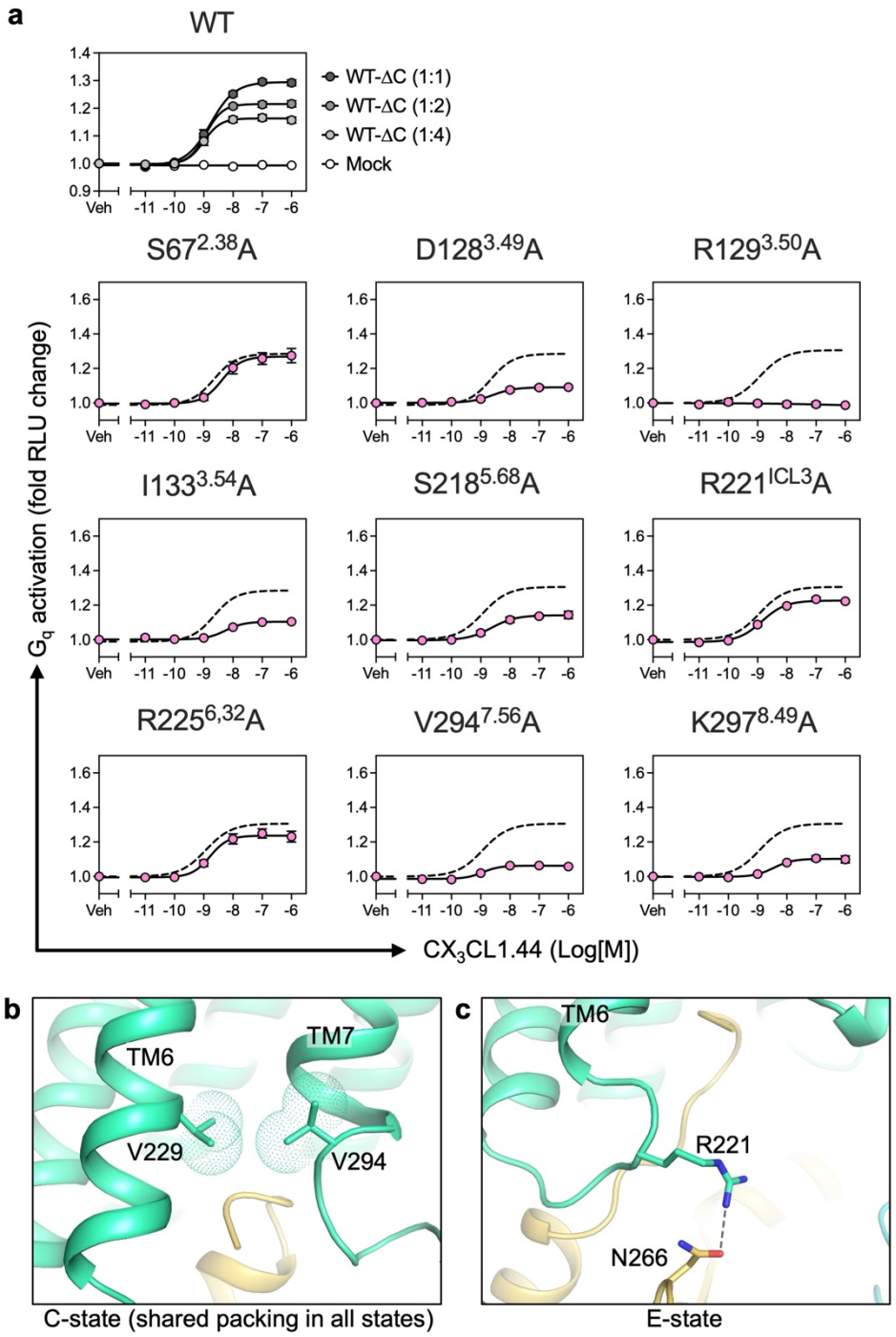

Supplementary Fig. 8 | Dataset for the structure-guided mutagenesis analysis.
a, Concentration-response curves from the NanoBiT-G_q activation assay for US28Δ300 variants. Cells expressing the indicated mutants were stimulated with increasing concentrations of $CX_3CL1.44$. G_q activation was monitored by the proximity signal between $G\alpha_q$-LgBiT and PLCβ2-SmBiT, measured as the fold change in relative luminescence units (RLU). Data represent the mean ± SEM from at least three independent experiments. Summarized results are shown in Fig. 4b. **b**, Val229-Val294 inter-helical packing in US28 shown in the C-state complex as an example. **c**, US28-Arg221:$G\alpha_q$-Asn266 hydrogen bond in the E-state.

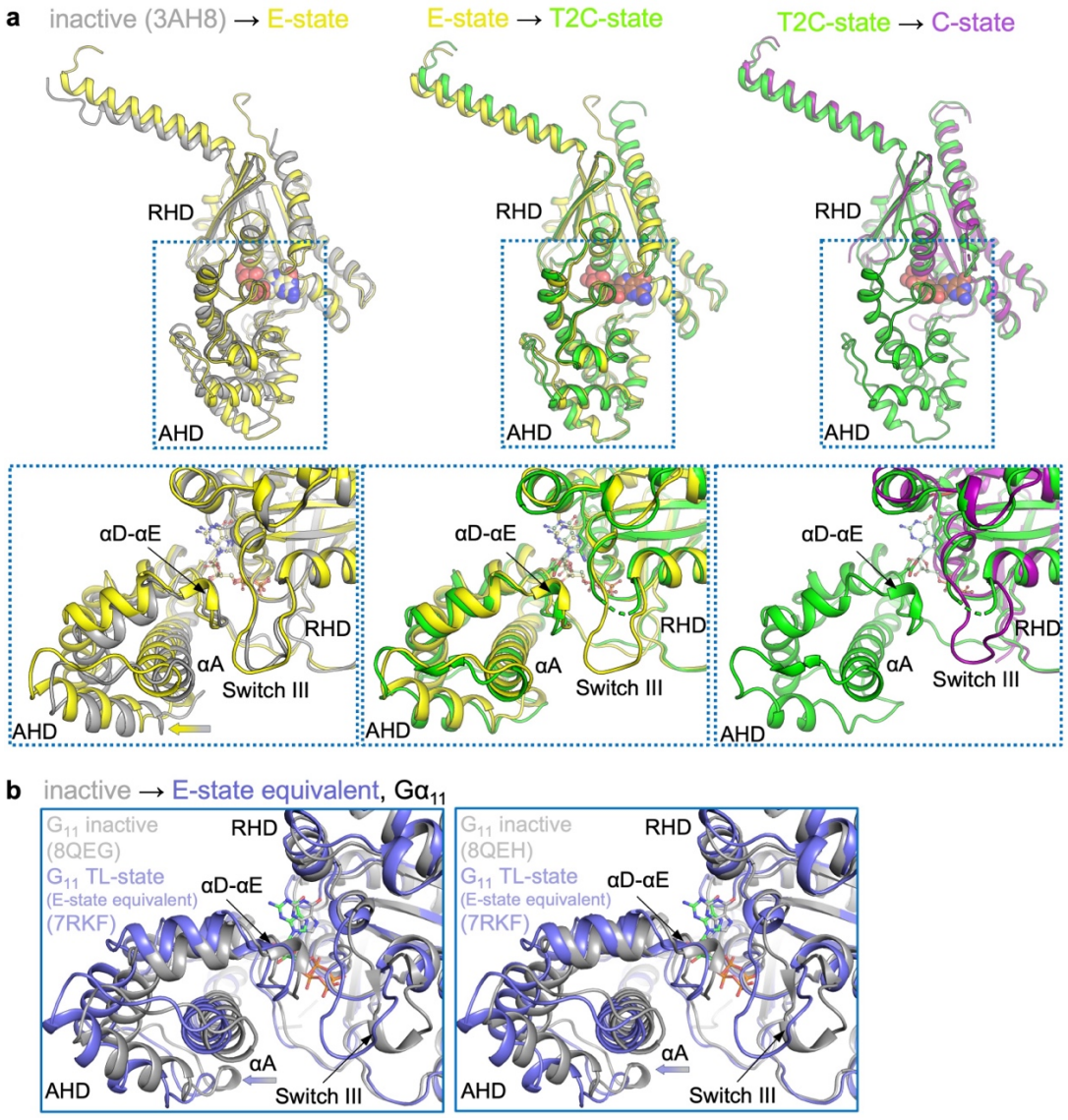

Supplementary Fig. 9 | Overall AHD motion relative to RHD during activation.

a, Structural comparison of $G\alpha_q$ showing the stepwise conformational changes leading to nucleotide release. Structures are aligned based on the RHD. (left) From the inactive to E-state, showing the slight shift for priming. (center) From the E- to T2C-states, showing the altered interdomain lock involving Switch III. (right) From the T2C- to C-states, showing complete separation of AHD. **b**, Comparisons between the inhibitor-bound inactive G_{11} (gray; PDB: 8QEG, left; 8QEH, right) and G_{11} in the TL-state CX_3CL1-US28-G_{11} complex (slate blue, PDB: 7RKF, equivalent of the E-state). Both panels are oriented to provide a close-up view of the RHD-AHD interface, highlighting the repositioning of Switch III and the αA helix during the transition from the inactive to the TL-state (or E-state).

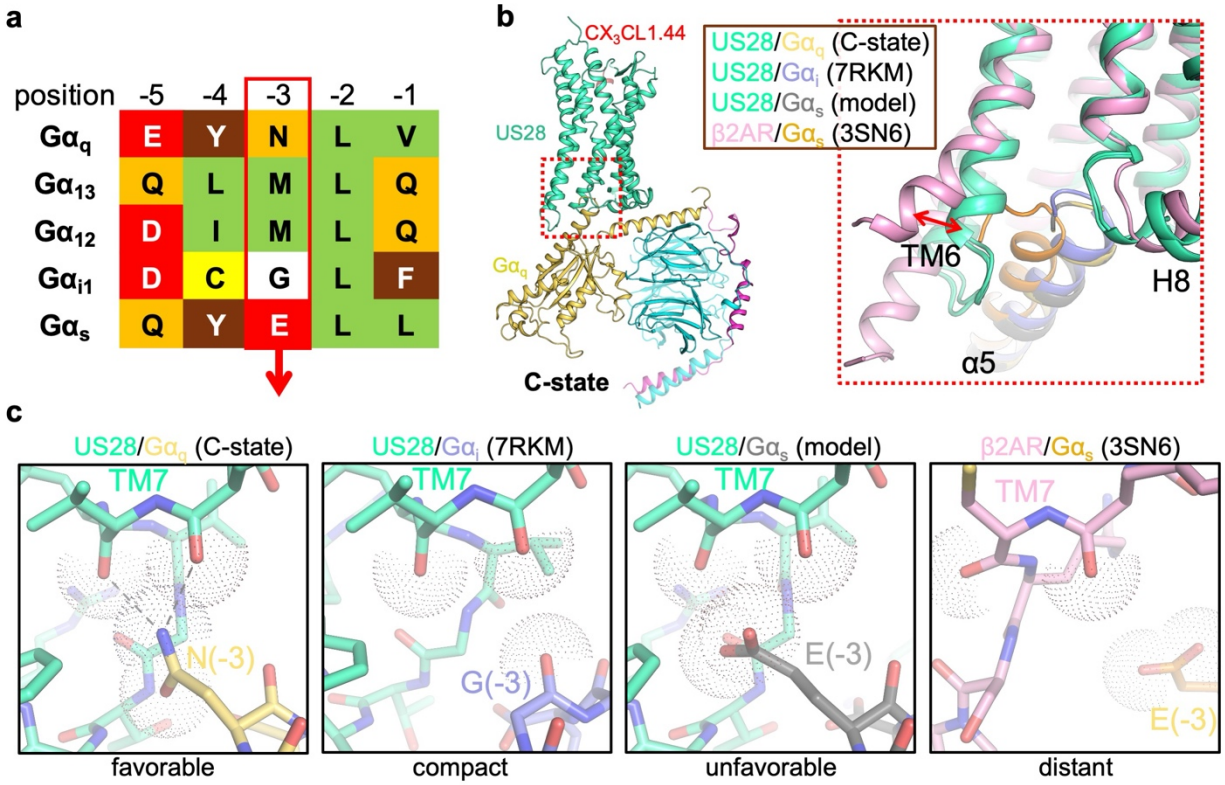

Supplementary Fig. 10 | Structural basis for G protein subtype selectivity by US28.
a, Sequence alignment of the C-terminal five residues of representative Gα subunits. Residues are color-coded by properties. $G\alpha_s$ uniquely possesses a glutamate at the -3 position. **b**, Structures of the C-state US28-G_q and US28-G_i complexes and a homology model of the US28-G_s complex (based on the C-state US28-G_q structure). **c**, Close-up views of the structures shown in panel b predict electrostatic repulsion between $G\alpha_s$-Glu(-3) and the backbone carbonyls at the intracellular end of US28 TM7, resulting from the receptor's relatively compact intracellular cavity. This contrasts with the US28-G_q complex, where Asn(-3) donates hydrogen bonds to the corresponding carbonyl, and the β2AR-G_s complex (PDB ID: 3SN6), where a wider opening accommodates the $G\alpha_s$ C-terminus.

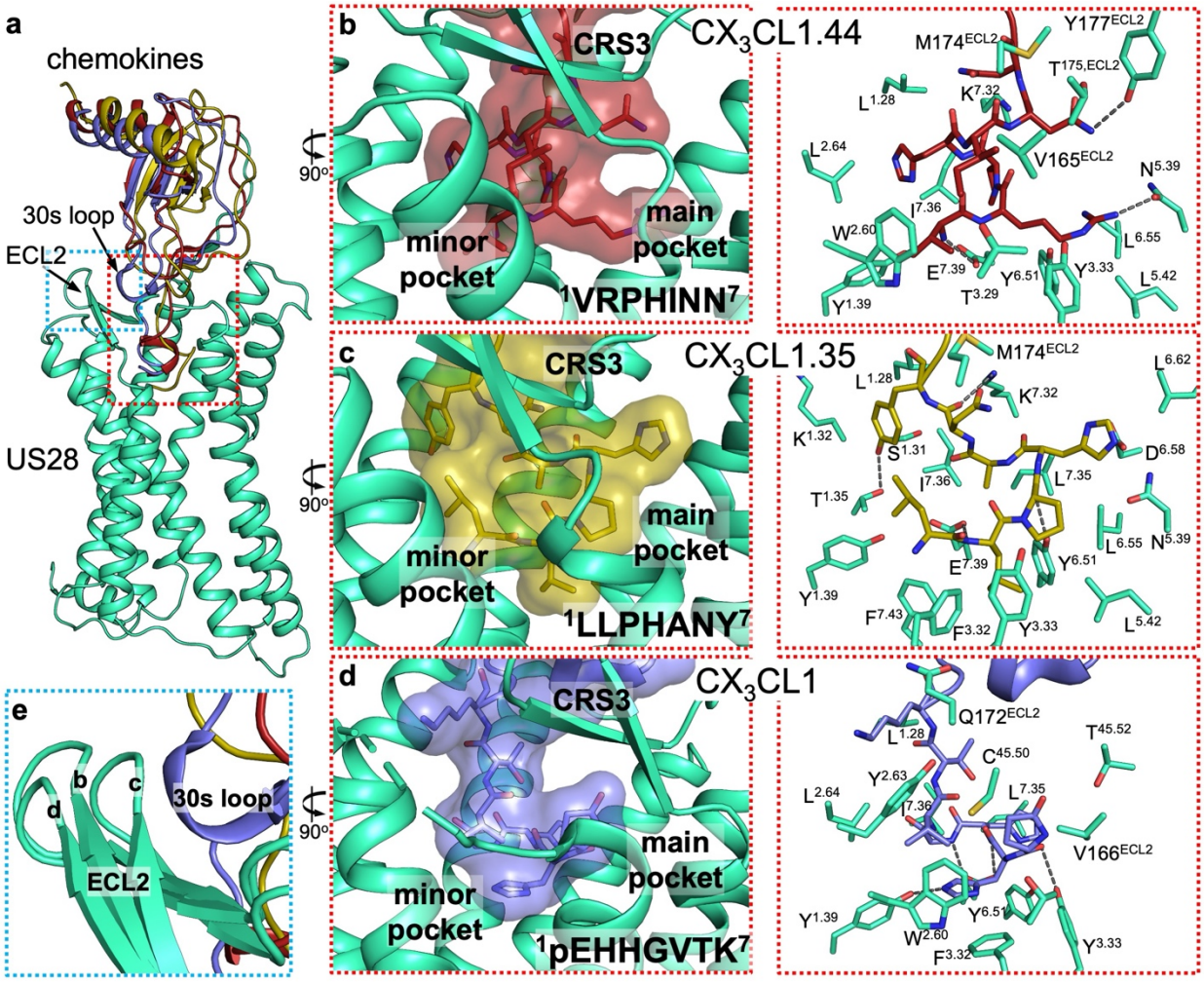

Supplementary Fig. 11 | Ligand engagement modes.

a, Overall binding modes of CX_3CL1 variants to US28. (**b**-**d**) Close-up views of the CRS2 interfaces between US28 and **b**, $CX_3CL1.44$ (red), **c**, $CX_3CL1.35$ (yellow), and **d**, wild-type CX_3CL1 (light blue). The N-terminal sequences of each chemokine are shown using one-letter codes; "pE" in panel d denotes pyroglutamate formed from the N-terminal glutamine residue. **e**, Comparison of the CRS3 interfaces between the three complexes. The labels b-d in panel e correspond to the structures shown in panels b-d.

Supplementary References

1. Tsutsumi, N. *et al.* Atypical structural snapshots of human cytomegalovirus GPCR interactions with host G proteins. *Sci. Adv.* **8**, eabl5442 (2022).
2. Jiao, H. *et al.* Structure basis for the modulation of CXC chemokine receptor 3 by antagonist AMG487. *Cell Discov.* **9**, 119 (2023).
3. Zhang, X. *et al.* Molecular basis for chemokine recognition and activation of XCR1. *Proc. Natl. Acad. Sci. U. S. A.* **121**, e2405732121 (2024).
4. Dror, R. O. *et al.* SIGNAL TRANSDUCTION. Structural basis for nucleotide exchange in heterotrimeric G proteins. *Science* **348**, 1361–1365 (2015).
5. Sun, X., Singh, S., Blumer, K. J. & Bowman, G. R. Simulation of spontaneous G protein activation reveals a new intermediate driving GDP unbinding. *Elife* **7**, (2018).
6. Rosenkilde, M. M., Tsutsumi, N., Knerr, J. M., Kildedal, D. F. & Garcia, K. C. Viral G protein-coupled receptors encoded by β- and γ-herpesviruses. *Annu. Rev. Virol.* **9**, 329–351 (2022).
7. Tsutsumi, N. *et al.* Insight into structural properties of viral G protein-coupled receptors and their role in the viral infection: IUPHAR Review 41. *Br. J. Pharmacol.* **182**, 26–51 (2025).
8. Waterhouse, A. *et al.* SWISS-MODEL: homology modelling of protein structures and complexes. *Nucleic Acids Res.* **46**, W296–W303 (2018).
9. Rasmussen, S. G. F. *et al.* Crystal structure of the β2 adrenergic receptor-Gs protein complex. *Nature* **477**, 549–555 (2011).
10. Flock, T. *et al.* Selectivity determinants of GPCR-G-protein binding. *Nature* **545**, 317–322 (2017).
11. Casiraghi, M. *et al.* Structure and dynamics determine G protein coupling specificity at a class A GPCR. *Sci. Adv.* **11**, eadq3971 (2025).